NANO LETTERS

pubs.acs.org/NanoLett Letter

Micron Thick Colloidal Quantum Dot Solids

James Z. Fan,[‖] Maral Vafaie,[‖] Koen Bertens,[‖] Mykhailo Sytnyk, Joao M. Pina, Laxmi Kishore Sagar, Olivier Ouellette, Andrew H. Proppe, Armin Sedighian Rasouli, Yajun Gao, Se-Woong Baek, Bin Chen, Frédéric Laquai, Sjoerd Hoogland, F. Pelayo García de Arquer, Wolfgang Heiss, and Edward H. Sargent*

Cite This: https://dx.doi.org/10.1021/acs.nanolett.0c01614 Read Online

ACCESS | Metrics & More | Article Recommendations | Supporting Information

ABSTRACT: Shortwave infrared colloidal quantum dots (SWIR-CQDs) are semiconductors capable of harvesting across the AM1.5G solar spectrum. Today's SWIR-CQD solar cells rely on spin-coating; however, these films exhibit cracking once thickness exceeds ~500 nm. We posited that a blade-coating strategy could enable thick QD films. We developed a ligand exchange with an additional resolvation step that enabled the dispersion of SWIR-CQDs. We then engineered a quaternary ink that combined high-viscosity solvents with short QD stabilizing ligands. This ink, blade-coated over a mild heating bed, formed micron-thick SWIR-CQD films. These SWIR-CQD solar cells achieved short-circuit current densities (Jsc) that reach 39 mA cm^{-2}, corresponding to the harvest of 60% of total photons incident under AM1.5G illumination. External quantum efficiency measurements reveal both the first exciton peak and the closest Fabry−Perot resonance peak reaching approximately 80%—this is the highest unbiased EQE reported beyond 1400 nm in a solution-processed semiconductor.

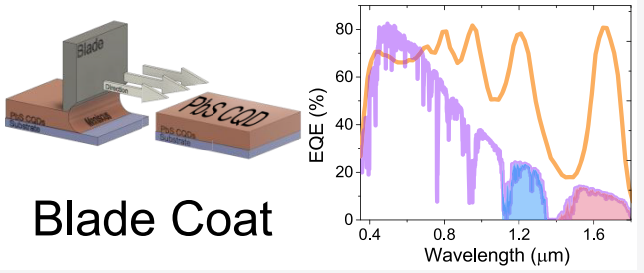

KEYWORDS: *infrared photovoltaics, quantum dots, ligand exchange, blade coating*

INTRODUCTION

Shortwave infrared (SWIR) semiconductors are materials capable of absorbing light between 1000 to 3000 nm. This region is of interest for applications including photodetection, light emission, and solar harvesting.[1] Operating photodetectors in the SWIR spectral range allows for the detection of light transmitted through biological (such as skin), atmospheric (such as water and CO_2), and synthetic materials (such as plastics).[2,3] Similarly, SWIR light emitting diodes (LEDs) are used in a variety of applications such as optical communications and night vision.[4,5] Finally, SWIR harvesting solar cells are excellent back cell candidates for visible absorbers such as silicon or metal halide perovskites.[6] Materials such as Ge, InGaAs, and HgCdTe alloys are excellent SWIR absorbers; however, their epitaxial incompatibility with silicon and flexible electronics and photovoltaics motivates the search for a new generation of materials.[7−9]

Colloidal quantum dots (CQDs) are a class of thin film semiconducting materials that can be synthesized in the solution phase.[10] Their band gap can be tuned to absorb more widely across the AM1.5G spectrum. In particular, SWIR-CQDs have been used to fabricate LEDs, photodetectors, and solar cells.[11−14] SWIR-CQD LEDs exhibit electroluminescence varying from 950 to 1650 nm, and their electroluminescence power is comparable to that of InGaAsP LEDs.[15] SWIR-CQD photodetectors have reached a detectivity of 10^{12} Jones at 2 μm.[16] SWIR-CQD solar cells have exhibited appreciable external quantum efficiencies up to 1800 nm.[17]

In recent years, research interest has increased in the optimization of SWIR-CQD PV for tandem integration with wide band gap front cells.[14,17−27] Infrared solar cell metrics such as IR-open circuit voltage (IR-Voc), IR-short circuit current density (IR-Jsc), IR-fill factor (IR-FF), and IR-power conversion efficiency (IR-PCE) are for solar cell operation through a simulated 1100 nm long pass filter. Innovations in SWIR-CQD synthesis and ligand engineering lead to improvements in IR power conversion efficiency (IR-PCE) metrics such as IR-open circuit voltage (IR-Voc).[17,28] However, the IR-short circuit current densities (IR-Jsc) of IR devices remain low due to inadequate absorption in the IR region.

Improving absorbance in the SWIR region requires increasing the thickness of the absorbing layer and broadening the absorption range of the semiconductor. Both aspects will significantly increase the maximum IR-Jsc, a main contributor for improving IR-PCE. The total available AM1.5G Jsc for 1.1 and 0.7 eV semiconductors are 44.23 mA cm^{-2} and 60.70 mA

Received: April 14, 2020
Revised: June 12, 2020
Published: June 16, 2020

https://dx.doi.org/10.1021/acs.nanolett.0c01614
Nano Lett. XXXX, XXX, XXX−XXX

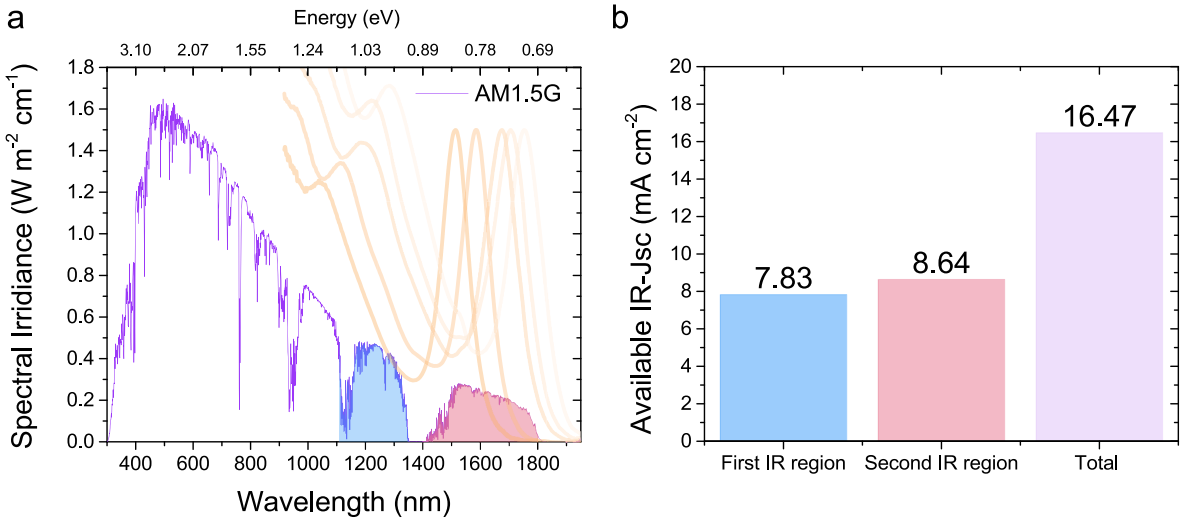

Figure 1. CQDs needed for full AM1.5G harvesting. Absorbance of shortwave infrared quantum dots overlaid on top of the AM1.5G to show potential IR harvesting (a). Available IR-short circuit current densities in the infrared region of the AM1.5G spectrum (b).

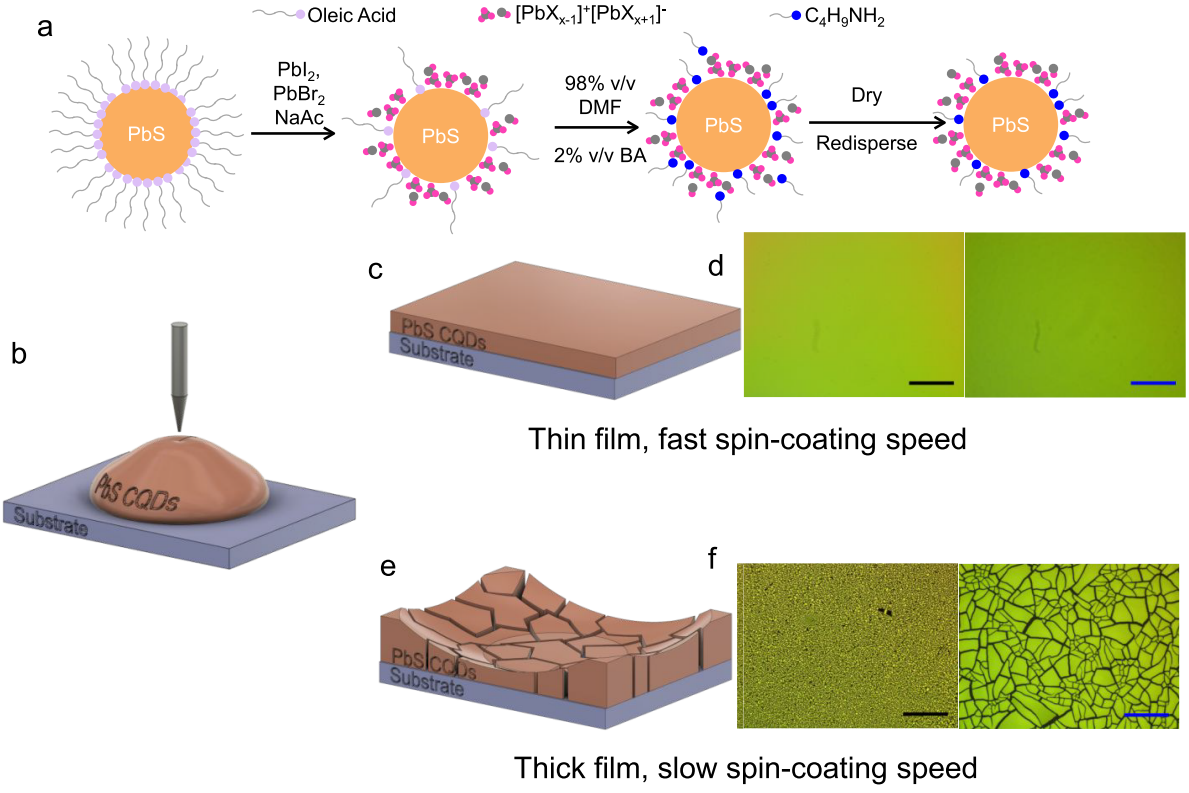

Figure 2. Ligand exchange and film processing. Ligand exchange for SWIR-CQDs with a double precipitation step (a); initial spin-coating schematic; (b) smooth thin film schematic enabled by rapid spin-coating (c); microscope image of the thin spin-coated film (d); cracked thick film schematic enabled by slow spin-coating (e); microscope image of the thick spin-coated film (f). Black scale bars represent 500 μm. Blue scale bars represent 50 μm.

cm^{-2}, respectively.[29] Therefore, this only results in a 37% increase in total Jsc. However, the visible wavelengths are mostly absorbed by the front cell; therefore, only the IR regions are of interest for tandem back cells. Harvesting the first IR-region between 1.1 eV (~1.1 μm) to 0.9 eV (~1.4 μm) results in an IR-Jsc of 7.83 mA cm^{-2}, while harvesting only the second IR-region between 0.9 eV (~1.4 μm) to 0.7 eV (~1.8 μm) results in an IR-Jsc of 8.64 mA cm^{-2}. By successfully harvesting both IR regions, devices can reach an IR-Jsc of 16.47 mA cm^{-2}: a doubling of Jsc (Figure 1a, b). By plotting several SWIR-CQD solution absorbance overlapping with the AM1.5G spectrum, we observe that the SWIR-CQDs ranging between $\lambda_{exciton}$ = ~1500 nm and $\lambda_{exciton}$ = ~1750 nm are capable of harvesting both IR regions. Prior work has demonstrated external quantum efficiencies (EQEs) that reached 80% in the first IR region.[25] In addition, EQEs have reached greater than 50% above the second IR region; however, their nearest Fabry−Perot resonance peak over-

https://dx.doi.org/10.1021/acs.nanolett.0c01614
Nano Lett. XXXX, XXX, XXX−XXX

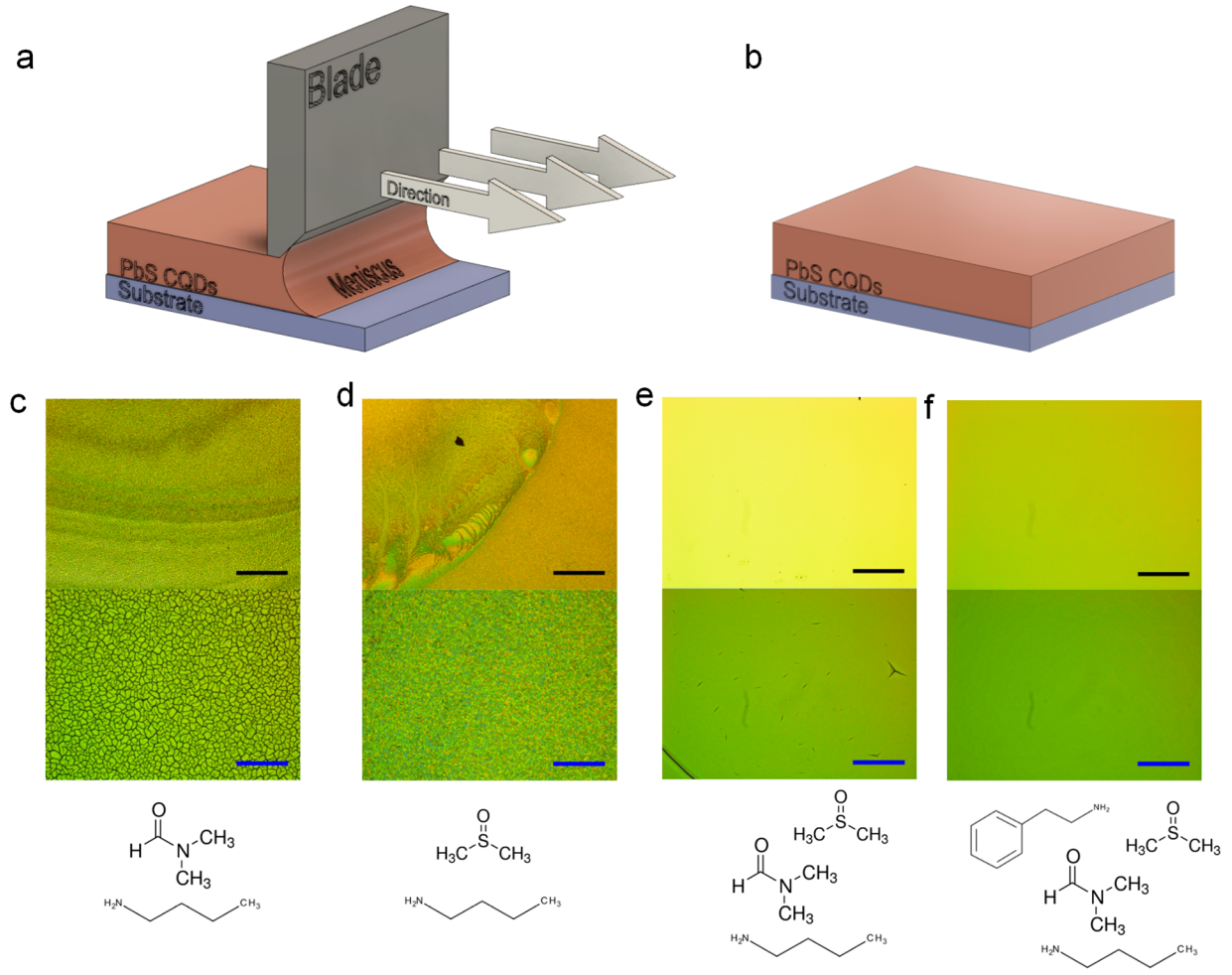

Figure 3. Blade-coating of SWIR CQDs. Blade-coating schematic (a, b). Microscope images of films made with blade-coating solvents composed of DMF and BA (c); DMSO and BA (d); DMF, DMSO, and BA (e); DMF, DMSO, PEA, and BA (f). Black scale bars represent 500 μm. Blue scale bars represent 50 μm.

lapped detrimentally with the first IR region, causing losses in Jsc.[23]

Here we demonstrate full AM1.5G harvesting SWIR-CQD solar cells that are capable of harvesting ~60% of all available solar photons.[29] We achieve this by implementing the combination of a new ligand exchange, solvent engineering, and blade-coating strategy. The new solvent engineering and blade-coating strategy allows the formation of smooth micron-thick CQD active layers. The combination of all three techniques results in CQD solar cells achieving the thickest reported PbS-CQD solar cell capable of reaching 80% external quantum efficiency with both the first exciton peak and nearest Fabry−Perot resonance peak in the infrared region between 1100 and 1800 nm—a feat that has not been achieved in the field of QD solar cells.

RESULTS AND DISCUSSION

The ligand exchange and ink deposition for single step SWIR-CQDs was previously challenging for the CQD community, as these QDs behave much differently than ligand exchanges optimized for single junction harvesting QDs (SJ-QDs, $\lambda_{exciton}$ = 900 to 1000 nm).[20] The specific procedure is described in the Supporting Information, but key differences for processing SJ-QDs and SWIR-CQDs are discussed here. SWIR-CQDs agglomerate immediately following phase transfer from the nonpolar octane phase to the halide-rich DMF phase, while SJ-QDs retain their colloidal stability. It is known that larger diameter SWIR-CQDs have higher amounts of Pb (100) facets than SJ-QDs.[30] As a consequence, these SWIR-CQDs are less colloidally stabilized by lead halides in the DMF phase. After the ligand exchange, several modifications must be made to successfully disperse the QDs into a concentrated ink. For the SJ-QD procedure, the exchanged QDs are first destabilized in the DMF phase with an antisolvent such as toluene. Then, the SJ-QDs are centrifuged, dried into a powder, and then dispersed into a solvent such as butylamine (BA). Translating this procedure for SWIR-CQDs does not work, as the SWIR-CQD powders do not disperse in butylamine, preventing film formation.

To overcome this issue, we implemented a double-precipitation step to enable the redispersion of the SWIR-CQDs (Figure 2a). After the completion of the ligand exchange procedure, the destabilized SWIR-CQDs were centrifuged and the supernatant was discarded. Then, the moist QDs were first resolvated in a solution of 98:2 v/v DMF/BA mixture. The low amount of BA was needed to stabilize the otherwise aggregated CQDs by exchanging the remaining oleic acid bound to the surface. The toluene antisolvent was added to the solution, and then the mixture was centrifuged. After the supernatant was discarded, the

https://dx.doi.org/10.1021/acs.nanolett.0c01614
Nano Lett. XXXX, XXX, XXX−XXX

SWIR-CQDs were dried and ready for redispersion. It is not possible to combine the phase transfer ligand exchange and resolvation process into one step. This is because adding the OA-PbS CQDs directly into a mixture of a concentrated ligand exchange solution containing a high percentage of redispersion solvent such as butylamine will not allow the efficient phase separation of octane and DMF. This will result in excess oleic acid to disperse in the single mixture, making blade or spin coating result in poor quality films for optoelectronic device fabrication.

Thermogravimetric analysis (TGA) revealed the reasoning for the double precipitation step (Supporting Figure S1a). After the first centrifuge, the QDs retained a lot of organic content on the surface of the QD, as indicated by the faster weight loss with increasing temperature. This is attributed to excess oleic acid still bound to the QDs. Since these QDs are passivated by both ionic salts and nonpolar species, these SWIR-CQDs fail to redisperse in traditional QD solvents. After the resolvation step, the organic content on the surface of the QDs significantly dropped, making these QDs mostly passivated with ionic species. Fourier transform infrared (FTIR) spectroscopy characterization on these singly precipitated SWIR-CQD films—materials that dispersed poorly in butylamine—further confirms the presence of organic residue (Supporting Figure S1b, S1c). The signals between 1200−1500 and 1080 cm^{-1} match closely those of OA-PbS CQDs and −NH bends from free butylamine, respectively.

A singular solvent approach, such as the use of butylamine, does not disperse the SWIR-CQDs, and attempting to deposit this ink leads to QD clusters over the film, making this unsuitable for devices (Supporting Figure S2). Therefore, SWIR-CQDs need to be dispersed in a combination of butylamine and DMF. We empirically found that a 30% mixture of DMF in butylamine was sufficient to create a stable SWIR-CQD colloid, similar to that of previous reports.[19,21,22] This solvent composition is adequate for spin-coating; the high amount of butylamine allows the majority of solvent to evaporate during the spin-coating process. Spin-coating the QDs at high speeds (>1000 rpm (RPM)) allowed for the formation of thin, smooth films (Figure 2c, d). However, this solvent composition only allows the formation of films up to ∼500 nm. This thickness is inadequate for infrared absorption, decreasing the overall performance of the solar cell. Spin-coating at lower speeds (e.g., less than 500 rpm) does not work to achieve thicker films. As the QD ink reaches the edge of the film, adhesive forces pin the ink to the corners, resulting in a high QD concentration at the corners. As the solvent evaporates, the films crack resulting in uneven, cracked, macroscopically rough films (Figure 2e, f). These pinhole-containing films result in shorting of the device; thus, single-step spin-coated QD devices are limited, in practice, to a thickness of ca. ∼500 nm.

Consequently, we contemplated fabrication techniques such as spray coating, roll-to-roll printing, and doctor-blading to create thicker films.[8,31−33] Doctor-blading in particular is known for fabricating thick solution-processed perovskite solar cells (e.g., >1000 nm films).[34] However, the full potential for doctor-blading has not yet been exploited in CQD solar cells, as the PCEs of reported doctor-bladed solar cells still remain below their spin-coated counterparts.[35] In our work, we fully rework our CQD ink conditions for doctor-blading to enable thick film fabrication.

In the blade-coating process, the CQD ink was first deposited on the blade edge to form a meniscus between the substrate and the blade edge. The blade is subsequently dragged over the substrate, as shown in Figure 3 a, b. We blade-coated at high speeds (>25 mm/s) to enable film formation in the Landu−Levich regime.[34,36] After the initial coat, the QD ink was still wet on the substrate; therefore, additional heating was needed to evaporate off the excess solvent. To ensure uniform film formation, we performed this blade-coating process on a glass heat bed to enable even evaporation of the film. Without the heat bed, the resulting films contained island-like spots, but by using an underlying heat source, the film underwent an initial solidification which prevented further migration of the ink upon the substrate.[33] We initially tested blade coating with the standard dispersion of 30/70 DMF/BA; however, we noticed that the solvent dried too quickly and formed cracked films under the spin-coat optimized concentrations of ink (>250 $mg{\cdot}mL^{-1}$) (Figure 3c). At lower concentrations, we noticed that the film dried nonuniformly, resulting in a rough, macroscopic texture across the top of the film. In order to create a thick uniform film, we attempted to engineer the ink with higher boiling point solvents to slow down the evaporation of the film. We first sought to use a combination of dimethyl sulfoxide (DMSO) (boiling point = 189 °C) and butylamine to increase the boiling point of the colloid. However, this mixture did not properly disperse the SWIR-CQDs, and thus a PV-grade film cannot be made (Figure 3d). By combining the three solvents {DMF, DMSO, and BA}, a stable SWIR-CQD colloid was achieved. This solvent system alone provided improved blade-coated SWIR-CQD films.

However, this solvent system caused film cracking when we attempted to fabricate >1000 nm films (Figure 3e). Therefore, we incorporated a fourth component, phenethylamine (PEA), to our system. PEA improves the ink mixture for the following reasons: (1) PEA's high boiling point (195 °C) further slows down the evaporation of the SWIR-CQD mixture; (2) PEA's greater than 2-fold viscosity over DMSO strikes a balance between the rate of coating and ink solidification; (3) the primary amine on the PEA stabilizes the lead halide matrix around the SWIR-CQD.[35] This quaternary solvent system allows us to fabricate smooth QD films thicker than 1000 nm (Figure 3f). Zoomed in microscope images reveal minor differences between the triple solvent and quaternary solvent blade-coated films (Supporting Figure S3). Atomic force microscope (AFM) images also reveal a smooth film for the quaternary ink (Supporting Figure S4). AFM imaging could not be completed for films shown in Figure 3c to 3e because those films were too rough to be imaged. The fabrication was finalized by an oven annealing step within a controlled atmosphere of nitrogen at 80 °C for 15 min to ensure that there was no residual solvent left. Transmission electron microscope (TEM) images reveal that the PbS CQDs remain monodisperse in the quaternary solvent system (Supporting Figure S5).

Additional characterization techniques such as X-ray photoelectron spectroscopy (XPS) and FTIR were used to compare blade-coated and spin-coated films (Supporting Figures S6−S8). FTIR showed similar features for both the spin-coated and blade-coated samples. There are no additional organic peaks seen on the blade-coated films compared to the spin-coated films. The loss of the C═C stretch at ∼3006 cm^{-1} is indicative of the successful removal of oleate ligands (Supporting Figure

https://dx.doi.org/10.1021/acs.nanolett.0c01614
Nano Lett. XXXX, XXX, XXX−XXX

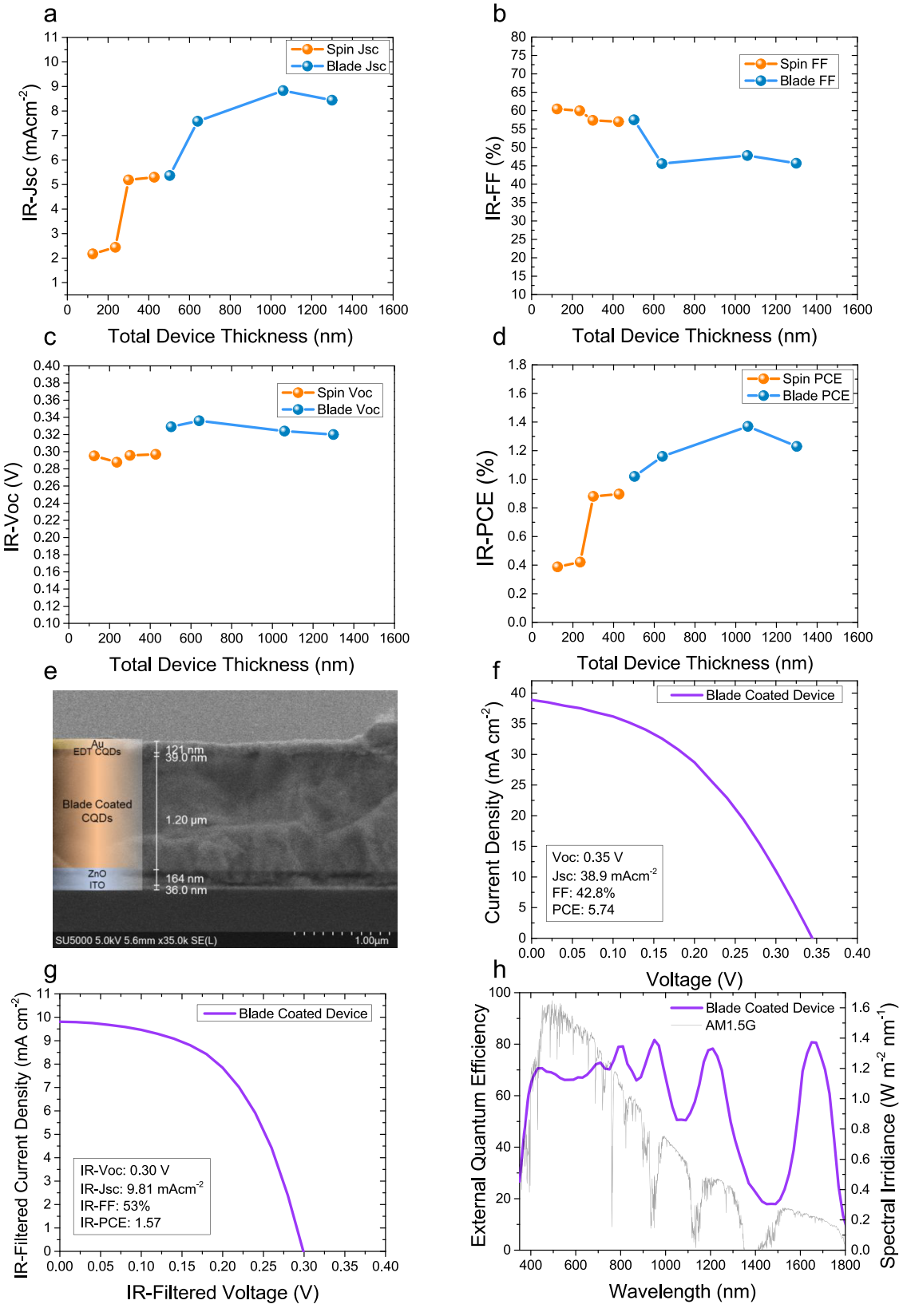

Figure 4. Solar cell metrics. Filtered solar cell parameters with varying thicknesses for IR-Jsc (a), IR-FF (b), IR-Voc (c), and IR-PCE (d). Cross section scanning electron microscope image of a blade-coated device (e). Full spectrum $J-V$ curve of champion blade-coated device (f). IR-filtered $J-V$ curve of champion blade-coated device (g). External quantum efficiency of champion blade-coated device (h).

S8a).[37,38] The Pb−amine complex is observed at ∼3484 cm^{-1} on both spin-coated and blade-coated films.[40] The signal between 1240 cm^{-1} and 1640 cm^{-1} correspond to the −NH bends from the Pb−amine complex, similar to a previous report (Supporting Figure S8b).[39] XPS was used to study the degree of passivation for the SWIR-CQD films (Supporting

https://dx.doi.org/10.1021/acs.nanolett.0c01614
Nano Lett. XXXX, XXX, XXX−XXX

Figures S6, S7a–d). Blade-coated films showed much higher iodide to sulfur and lead to sulfur ratios, indicting better passivation of the QD. We suspect that the addition of both DMSO and PEA stabilizes residual PbX_2 (X = I, Br) species on the QD surface, thus increasing the amount of both I/S and Pb/S ratios.[40]

Finally, we fabricated IR harvesting solar cells using both techniques. We used an ITO/ZnO/PbX-PbS/EDT-PbS/Au architecture for the devices. Infrared solar cell metrics such as IR-open circuit voltage (IR-Voc), IR-short circuit current density (IR-Jsc), IR-fill factor (IR-FF), and IR-power conversion efficiency (IR-PCE) were compared for different thicknesses of both spin-coated and blade-coated samples (Figure 4a–d). The PCE metrics under AM1.5G illumination are presented in Supporting Figure S9. A representative cross-sectional scanning electron microscope (SEM) image reveals a continuous SWIR CQD layer exceeding 1 μm (Figure 4e). The active layer thicknesses for spin-coated devices varied between ~130 and 430 nm, while the blade-coated active layer thicknesses ranged from 500 nm to 1.3 μm. Our blade-coating solvent was optimized to favor thicker active layers; as a result, blade coating does not produce high-quality sub-500 nm devices. Indeed, fabricating thin blade-coated films require slow coating speeds, leading to the uneven evaporation of CQD solvent. Even if we did reoptimize our blade-coating QD inks for thinner films, the lower absorbance of the active layer is unfavorable for increasing the overall PCE. As mentioned earlier, spin-coated devices above 500 nm showed significant signs of cracking; therefore, we were not able to successfully fabricate thicker spin-coated devices.

The IR-Jsc of these devices showed an upward increase as the thickness of the active layer increased. This is expected, as the absorbance of the device increases with thickness. Selected external quantum efficiency (EQE) spectra reveal the phenomena for the rapid increase in Jsc (Supporting Figure S10). As expected, the first exciton peak generally increases with active layer thickness. Interestingly, the gap between the first exciton peak and the closest Fabry–Perot resonance peak becomes favorably narrower with increasing active layer thickness. The overlap between the Fabry–Perot resonance peak and the first IR region is mainly responsible for the large increases with Jsc. Jsc does not increase monotonically as seen in other recent studies.[17,18,41] In our case, when the spin-coated film increased from ca. 300 to 430 nm, there was a slight drop in Jsc (Supporting Figure S9).

The IR-FF decreased with increasing thicknesses, which is a result of increased carrier recombination for thicker devices (Figure 4b). The *JV* curves of the blade-coated sample show the IR-FF gradually decreasing with thickness (Supporting Figure S11a). In addition, the IR-power density vs voltage curves and IR-maximum power point also shift toward lower voltages with increasing thickness—indicative of the slight decrease in IR-FF (Supporting Figure S11b). Interestingly, the IR-Voc was higher for the blade-coated set. We hypothesized that film formation as a result of blade coating improved the solid state QD dispersity. The absorbance of the blade-coated films showed a narrower fwhm than the spin-coated ones (Supporting Figure S12). Blade-coated films also have a lower film Stokes shift of 19 meV compared to a spin-coated film Stokes shift of 62 meV. A lower Stokes shift is indicative of improved film monodispersity, leading to flatter energy landscapes and higher built-in potentials.[14,42] The champion *J–V* curve under full AM1.5G illumination has a Jsc of 38.9 $mAcm^{-2}$, currently the highest Jsc for all solution processed, thin film solar cells (Figure 4f). This Jsc value also accounts for approximately 60% of total solar photons under AM1.5G illumination.[29] The IR-Jsc also reaches 9.81 $mAcm^{-2}$, 70% greater than that of previously reported IR-CQD solar cells (Figure 4g).[17,28] The unbiased EQE showed both the first exciton peak at ~1670 nm reaching ~80%, and the nearest Fabry–Perot resonance peak at ~1210 nm approaching 80% (Figure 4h). The exciton peak at 1670 nm exceeds previous CQD EQE exciton peaks by over 30% and is comparable to EQE values from single crystalline Ge solar cells in this IR region.[17,43,44] This work presents the highest unbiased EQE for all solution-processed semiconductor ranges beyond 1400 nm, suggesting further applications for IR detection.[3,45,46]

In conclusion, we utilized the full advantage of blade coating to create thick, smooth CQD films. Previous spin-coating methods caused significant cracking upon attempting to increase thickness. By engineering a four-component high boiling viscous CQD ink, we could readily fabricate micron thick PbS CQD active layers. These thick layers offer incredible improvements in IR-harvesting mainly due to the favorable matching of both the first exciton peak and nearest Fabry–Perot peak to the AM1.5G spectrum. These blade-coated CQD devices harvest the entire solar spectrum, providing one more step toward the fabrication of triple and quad-junction solar cells.

■ ASSOCIATED CONTENT

Supporting Information

The Supporting Information is available free of charge at https://pubs.acs.org/doi/10.1021/acs.nanolett.0c01614.

Experimental Methods, TGA, microscope images, XPS, *J–V* curves, EQE spectra, absorbance, and PL data (PDF)

■ AUTHOR INFORMATION

Corresponding Author

Edward H. Sargent – *Department of Electrical and Computer Engineering, University of Toronto, Toronto, Ontario M5S 3G4, Canada;* orcid.org/0000-0003-0396-6495; Email: ted.sargent@utoronto.ca

Authors

James Z. Fan – *Department of Electrical and Computer Engineering, University of Toronto, Toronto, Ontario M5S 3G4, Canada;* orcid.org/0000-0002-1594-865X

Maral Vafaie – *Department of Electrical and Computer Engineering, University of Toronto, Toronto, Ontario M5S 3G4, Canada;* orcid.org/0000-0001-9119-6499

Koen Bertens – *Department of Electrical and Computer Engineering, University of Toronto, Toronto, Ontario M5S 3G4, Canada*

Mykhailo Sytnyk – *Materials for Electronics and Energy Technology (i-MEET), Department of Materials Science and Engineering, Friedrich-Alexander-Universität Erlangen-Nürnberg, Nürnberg 90429, Germany*

Joao M. Pina – *Department of Electrical and Computer Engineering, University of Toronto, Toronto, Ontario M5S 3G4, Canada;* orcid.org/0000-0002-3448-0028

Laxmi Kishore Sagar – *Department of Electrical and Computer Engineering, University of Toronto, Toronto, Ontario M5S 3G4, Canada;* orcid.org/0000-0002-7656-7308

https://dx.doi.org/10.1021/acs.nanolett.0c01614
Nano Lett. XXXX, XXX, XXX–XXX

Olivier Ouellette − *Department of Electrical and Computer Engineering, University of Toronto, Toronto, Ontario M5S 3G4, Canada;* orcid.org/0000-0001-5708-5058
Andrew H. Proppe − *Department of Electrical and Computer Engineering, University of Toronto, Toronto, Ontario M5S 3G4, Canada;* orcid.org/0000-0003-3860-9949
Armin Sedighian Rasouli − *Department of Electrical and Computer Engineering, University of Toronto, Toronto, Ontario M5S 3G4, Canada*
Yajun Gao − *King Abdullah University of Science and Technology (KAUST), KAUST Solar Center (KSC), Physical Sciences and Engineering Division (PSE), Material Science and Engineering Program (MSE), Thuwal 23955-6900, Saudi Arabia*
Se-Woong Baek − *Department of Electrical and Computer Engineering, University of Toronto, Toronto, Ontario M5S 3G4, Canada*
Bin Chen − *Department of Electrical and Computer Engineering, University of Toronto, Toronto, Ontario M5S 3G4, Canada*
Frédéric Laquai − *King Abdullah University of Science and Technology (KAUST), KAUST Solar Center (KSC), Physical Sciences and Engineering Division (PSE), Material Science and Engineering Program (MSE), Thuwal 23955-6900, Saudi Arabia;* orcid.org/0000-0002-5887-6158
Sjoerd Hoogland − *Department of Electrical and Computer Engineering, University of Toronto, Toronto, Ontario M5S 3G4, Canada*
F. Pelayo García de Arquer − *Department of Electrical and Computer Engineering, University of Toronto, Toronto, Ontario M5S 3G4, Canada;* orcid.org/0000-0003-2422-6234
Wolfgang Heiss − *Materials for Electronics and Energy Technology (i-MEET), Department of Materials Science and Engineering, Friedrich-Alexander-Universität Erlangen-Nürnberg, Nürnberg 90429, Germany;* orcid.org/0000-0003-0430-9550

Complete contact information is available at: https://pubs.acs.org/10.1021/acs.nanolett.0c01614

Author Contributions

[‖]J.Z.F., M.V., and K.B. contributed equally

Funding

This work was supported by Ontario Research Fund-Research Excellence program (ORF7 ministry of Research and Innovation, Ontario Research Fund-Research Excellence Round 7) and by the Natural Sciences and Engineering Research Council (NSERC) of Canada in the form of Alexander Graham Bell Canada Graduate Scholarships (CGS-D), Materials for Enhanced Energy Technologies (MEET) scholarships, and the NSERC Collaborative Research and Training Experience (CREATE) Program Grant Number 466083. The authors acknowledge financial support from QD Solar. This publication is also based upon work supported by the King Abdullah University of Science and Technology (KAUST) Office of Sponsored Research (OSR) under Award No. OSR-CRG2018-3737.

Notes

The authors declare no competing financial interest.

■ ACKNOWLEDGMENTS

The authors thank L. Levina, E. Palmiano, R. Wolowiec, and D. Kopilovic for their assistance during the period of study. The authors also thank the members of QD Solar for their assistance and discussions during the period of study: V. Tran, T. Vo, T. Gibbs, M. Labine, A. MacDonald, E. Mosaferi, R. Quintero-Bermudez, and A. Fisher.

■ ABBREVIATIONS

Short wave infrared (SWIR); Colloidal Quantum Dot (CQD); Infrared (IR); Single junction (SJ); Butylamine (BA); Theromgravimetric analysis (TGA); Dimethyl sulfoxide (DMSO); X-ray Photoelectron Spectroscopy (XPS); Fourier Transform Infrared Spectroscopy (FTIR); Phenethylamine (PEA); Scanning electron microscope (SEM); Open circuit voltage (Voc); Short circuit current density (Jsc); Fill factor (FF); Power conversion efficiency (PCE); Full width at half-maximum (fwhm)

■ REFERENCES

(1) García De Arquer, F. P.; Armin, A.; Meredith, P.; Sargent, E. H. Solution-Processed Semiconductors for next-Generation Photodetectors. *Nat. Rev. Mater.* **2017**, *2* (3), 1−16.
(2) Wilson, R. H.; Nadeau, K. P.; Jaworski, F. B.; Tromberg, B. J.; Durkin, A. J. Review of Short-Wave Infrared Spectroscopy and Imaging Methods for Biological Tissue Characterization. *J. Biomed. Opt.* **2015**, *20* (3), 030901.
(3) Clifford, J. P.; Konstantatos, G.; Johnston, K. W.; Hoogland, S.; Levina, L.; Sargent, E. H. Fast, Sensitive and Spectrally Tuneable Colloidal-Quantum-Dot Photodetectors. *Nat. Nanotechnol.* **2009**, *4* (1), 40−44.
(4) Jeon, E. S.; Kim, J. H.; Hong, H. G.; Batchuluun, G.; Park, K. R. Human Detection Based on the Generation of a Background Image and Fuzzy System by Using a Thermal Camera. *Sensors* **2016**, *16* (4), 453.
(5) Hansen, M. P.; Malchow, D. S. Overview of SWIR Detectors, Cameras, and Applications. *Proc. SPIE* **2008**, *6939* (March 2008), 69390I.
(6) Lumb, M. P.; Mack, S.; Schmieder, K. J.; González, M.; Bennett, M. F.; Scheiman, D.; Meitl, M.; Fisher, B.; Burroughs, S.; Lee, K. T.; et al. GaSb-Based Solar Cells for Full Solar Spectrum Energy Harvesting. *Adv. Energy Mater.* **2017**, *7* (20), 1700345.
(7) Leem, J. W.; Yu, J. S.; Kim, J. N.; Noh, S. K. Theoretical Modeling and Optimization of III-V GaInP/GaAs/Ge Monolithic Triple-Junction Solar Cells. *J. Korean Phys. Soc.* **2014**, *64* (10), 1561−1565.
(8) Kramer, I. J.; Moreno-Bautista, G.; Minor, J. C.; Kopilovic, D.; Sargent, E. H. Colloidal Quantum Dot Solar Cells on Curved and Flexible Substrates. *Appl. Phys. Lett.* **2014**, *105* (16), 163902.
(9) Norton, P. HgCdTe Infrared Detectors. *Opto-electronics Rev.* **2002**, *10* (3), 159−174.
(10) Wang, R.; Shang, Y.; Kanjanaboos, P.; Zhou, W.; Ning, Z.; Sargent, E. H. Colloidal Quantum Dot Ligand Engineering for High Performance Solar Cells. *Energy Environ. Sci.* **2016**, *9* (4), 1130−1143.
(11) Yan, L.; Shen, X.; Zhang, Y.; Zhang, T.; Zhang, X.; Feng, Y.; Yin, J.; Zhao, J.; Yu, W. W. Near-Infrared Light Emitting Diodes Using PbSe Quantum Dots. *RSC Adv.* **2015**, *5* (67), 54109−54114.
(12) Yang, Z.; Voznyy, O.; Liu, M.; Yuan, M.; Ip, A. H.; Ahmed, O. S.; Levina, L.; Kinge, S.; Hoogland, S.; Sargent, E. H. All-Quantum-Dot Infrared Light-Emitting Diodes. *ACS Nano* **2015**, *9* (12), 12327−12333.
(13) Tang, H.; Zhong, J.; Chen, W.; Shi, K.; Mei, G.; Zhang, Y.; Wen, Z.; Müller-Buschbaum, P.; Wu, D.; Wang, K.; et al. Lead Sulfide Quantum Dot Photodetector with Enhanced Responsivity through a Two-Step Ligand-Exchange Method. *ACS Appl. Nano Mater.* **2019**, *2* (10), 6135−6143.
(14) Ip, A. H.; Kiani, A.; Kramer, I. J.; Voznyy, O.; Movahed, H. F.; Levina, L.; Adachi, M. M.; Hoogland, S.; Sargent, E. H. Infrared Colloidal Quantum Dot Photovoltaics via Coupling Enhancement and Agglomeration Suppression. *ACS Nano* **2015**, *9* (9), 8833−8842.

(15) Hyun, B.-R.; Malliaras, G. G.; Wise, F. W.; Hanrath, T.; Choi, J. J.; Sun, L.; Stachnik, D.; Bartnik, A. C. Bright Infrared Quantum-Dot Light-Emitting Diodes through Inter-Dot Spacing Control. *Nat. Nanotechnol.* **2012**, *7* (6), 369−373.
(16) Huo, N.; Gupta, S.; Konstantatos, G. MoS2−HgTe Quantum Dot Hybrid Photodetectors beyond 2 Mm. *Adv. Mater.* **2017**, *29* (17), 1606576.
(17) Bi, Y.; Bertran, A.; Gupta, S.; Ramiro, I.; Pradhan, S.; Christodoulou, S.; Majji, S.; Akgul, Z.; Konstantatos, G. Solution Processed Infrared- and Thermo- Photovoltaics Based on 0.7 EV Bandgap PbS Colloidal Quantum Dots. *Nanoscale* **2019**, *11* (3), 838−843.
(18) Sun, B.; Ouellette, O.; de Arquer, F. P. G.; Voznyy, O.; Kim, Y.; Wei, M.; Proppe, A. H.; Saidaminov, M. I.; Xu, J.; Liu, M.; et al. Multibandgap Quantum Dot Ensembles for Solar-Matched Infrared Energy Harvesting. *Nat. Commun.* **2018**, *9* (1), 1−7.
(19) Fan, J. Z.; Andersen, N. T.; Biondi, M.; Todorović, P.; Sun, B.; Ouellette, O.; Abed, J.; Sagar, L. K.; Choi, M.; Hoogland, S.; et al. Mixed Lead Halide Passivation of Quantum Dots. *Adv. Mater.* **2019**, *31* (48), 1904304.
(20) Kiani, A.; Sutherland, B. R.; Kim, Y.; Ouellette, O.; Levina, L.; Walters, G.; Dinh, T.; Liu, M.; Voznyy, O.; Lan, X.; et al. Single-Step Colloidal Quantum Dot Films for Infrared Solar Harvesting. *Appl. Phys. Lett.* **2016**, *109* (18), 183105.
(21) Fan, J. Z.; Liu, M. M.; Voznyy, O.; Sun, B.; Levina, L.; Quintero-Bermudez, R.; Liu, M. M.; Ouellette, O.; García de Arquer, F. P.; Hoogland, S.; et al. Halide Re-Shelled Quantum Dot Inks for Infrared Photovoltaics. *ACS Appl. Mater. Interfaces* **2017**, *9* (43), 37536−37541.
(22) Kim, Y.; Che, F.; Jo, J. W.; Choi, J.; García de Arquer, F. P.; Voznyy, O.; Sun, B.; Kim, J.; Choi, M.-J.; Quintero-Bermudez, R.; et al. A Facet-Specific Quantum Dot Passivation Strategy for Colloid Management and Efficient Infrared Photovoltaics. *Adv. Mater.* **2019**, *31* (17), 1805580.
(23) Jo, J. W.; Choi, J.; García De Arquer, F. P.; Seifitokaldani, A.; Sun, B.; Kim, Y.; Ahn, H.; Fan, J.; Quintero-Bermudez, R.; Kim, J.; et al. Acid-Assisted Ligand Exchange Enhances Coupling in Colloidal Quantum Dot Solids. *Nano Lett.* **2018**, *18* (7), 4417−4423.
(24) Choi, J.; Jo, J. W.; de Arquer, F. P. G.; Zhao, Y. B.; Sun, B.; Kim, J.; Choi, M. J.; Baek, S. W.; Proppe, A. H.; Seifitokaldani, A.; et al. Activated Electron-Transport Layers for Infrared Quantum Dot Optoelectronics. *Adv. Mater.* **2018**, *30* (29), 1801720.
(25) Bi, Y.; Pradhan, S.; Gupta, S.; Akgul, M. Z.; Stavrinadis, A.; Konstantatos, G. Infrared Solution-Processed Quantum Dot Solar Cells Reaching External Quantum Efficiency of 80% at 1.35 Mm and Jsc in Excess of 34 MA Cm-2. *Adv. Mater.* **2018**, *30* (7), 1704928.
(26) Kim, J.; Ouellette, O.; Voznyy, O.; Wei, M.; Choi, J.; Choi, M.; Jo, J. W.; Baek, S.; Fan, J.; Saidaminov, M. I.; et al. Butylamine-Catalyzed Synthesis of Nanocrystal Inks Enables Efficient Infrared CQD Solar Cells. *Adv. Mater.* **2018**, *30* (45), 1803830.
(27) Baek, S. W.; Molet, P.; Choi, M. J.; Biondi, M.; Ouellette, O.; Fan, J.; Hoogland, S.; García de Arquer, F. P.; Mihi, A.; Sargent, E. H. Nanostructured Back Reflectors for Efficient Colloidal Quantum-Dot Infrared Optoelectronics. *Adv. Mater.* **2019**, *31* (33), 1901745.
(28) Xia, Y.; Liu, S.; Wang, K.; Yang, X.; Lian, L.; Zhang, Z.; He, J.; Liang, G.; Wang, S.; Tan, M.; et al. Cation-Exchange Synthesis of Highly Monodisperse PbS Quantum Dots from ZnS Nanorods for Efficient Infrared Solar Cells. *Adv. Funct. Mater.* **2020**, *30* (4), 1907379.
(29) Rühle, S. Tabulated Values of the Shockley-Queisser Limit for Single Junction Solar Cells. *Sol. Energy* **2016**, *130* (June 2016), 139−147.
(30) Choi, H.; Ko, J. H.; Kim, Y. H.; Jeong, S. Steric-Hindrance-Driven Shape Transition in PbS Quantum Dots: Understanding Size-Dependent Stability. *J. Am. Chem. Soc.* **2013**, *135* (14), 5278−5281.
(31) Kirmani, A. R.; Sheikh, A. D.; Niazi, M. R.; Haque, M. A.; Liu, M.; de Arquer, F. P. G.; Xu, J.; Sun, B.; Voznyy, O.; Gasparini, N.; et al. Overcoming the Ambient Manufacturability-Scalability-Performance Bottleneck in Colloidal Quantum Dot Photovoltaics. *Adv. Mater.* **2018**, *30* (35), 1870260.
(32) Aqoma, H.; Jang, S. Y. Solid-State-Ligand-Exchange Free Quantum Dot Ink-Based Solar Cells with an Efficiency of 10.9%. *Energy Environ. Sci.* **2018**, *11* (6), 1603−1609.
(33) Choi, M. J.; Kim, Y. J.; Lim, H.; Alarousu, E.; Adhikari, A.; Shaheen, B. S.; Kim, Y. H.; Mohammed, O. F.; Sargent, E. H.; Kim, J. Y.; et al. Tuning Solute-Redistribution Dynamics for Scalable Fabrication of Colloidal Quantum-Dot Optoelectronics. *Adv. Mater.* **2019**, *31* (32), 1805886.
(34) Deng, Y.; Zheng, X.; Bai, Y.; Wang, Q.; Zhao, J.; Huang, J. Surfactant-Controlled Ink Drying Enables High-Speed Deposition of Perovskite Films for Efficient Photovoltaic Modules. *Nat. Energy* **2018**, *3* (7), 560−566.
(35) Xu, J.; Voznyy, O.; Liu, M.; Kirmani, A. R.; Walters, G.; Munir, R.; Abdelsamie, M.; Proppe, A. H.; Sarkar, A.; García De Arquer, F. P.; et al. 2D Matrix Engineering for Homogeneous Quantum Dot Coupling in Photovoltaic Solids. *Nat. Nanotechnol.* **2018**, *13* (6), 456−462.
(36) Le Berre, M.; Chen, Y.; Baigl, D. From Convective Assembly to Landau - Levich Deposition of Multilayered Phospholipid Films of Controlled Thickness. *Langmuir* **2009**, *25* (5), 2554−2557.
(37) Zhang, X.; Cappel, U. B.; Jia, D.; Zhou, Q.; Du, J.; Sloboda, T.; Svanström, S.; Johansson, F. O. L.; Lindblad, A.; Giangrisostomi, E.; et al. Probing and Controlling Surface Passivation of PbS Quantum Dot Solid for Improved Performance of Infrared Absorbing Solar Cells. *Chem. Mater.* **2019**, *31* (11), 4081−4091.
(38) Albaladejo-Siguan, M.; Becker-Koch, D.; Taylor, A. D.; Sun, Q.; Lami, V.; Oppenheimer, P. G.; Paulus, F.; Vaynzof, Y. Efficient and Stable PbS Quantum Dot Solar Cells by Triple-Cation Perovskite Passivation. *ACS Nano* **2020**, *14* (1), 384−393.
(39) Acik, M.; Alam, T. M.; Guo, F.; Ren, Y.; Lee, B.; Rosenberg, R. A.; Mitchell, J. F.; Park, I. K.; Lee, G.; Darling, S. B. Substitutional Growth of Methylammonium Lead Iodide Perovskites in Alcohols. *Adv. Energy Mater.* **2018**, *8* (5), 1701726.
(40) Jeon, N. J.; Noh, J. H.; Kim, Y. C.; Yang, W. S.; Ryu, S.; Seok, S. Il. Solvent Engineering for High-Performance Inorganic-Organic Hybrid Perovskite Solar Cells. *Nat. Mater.* **2014**, *13* (9), 897.
(41) Lin, Q.; Armin, A.; Nagiri, R. C. R.; Burn, P. L.; Meredith, P. Electro-Optics of Perovskite Solar Cells. *Nat. Photonics* **2015**, *9* (2), 106−112.
(42) Liu, M.; Voznyy, O.; Sabatini, R.; García De Arquer, F. P.; Munir, R.; Balawi, A. H.; Lan, X.; Fan, F.; Walters, G.; Kirmani, A. R.; et al. Hybrid Organic-Inorganic Inks Flatten the Energy Landscape in Colloidal Quantum Dot Solids. *Nat. Mater.* **2017**, *16* (2), 258−263.
(43) Guter, W.; Schöne, J.; Philipps, S. P.; Steiner, M.; Siefer, G.; Wekkeli, A.; Welser, E.; Oliva, E.; Bett, A. W.; Dimroth, F. Current-Matched Triple-Junction Solar Cell Reaching 41.1% Conversion Efficiency under Concentrated Sunlight. *Appl. Phys. Lett.* **2009**, *94* (22), 223504.
(44) Grás, A.; Jüngst, G.; Campesato, R.; Gori, G.; Greco, E. External Quantum Efficiency and First Results of Electric Performance Measurements on a Quadruple Junction Space Solar Cell. *In E3S Web of Conferences* **2017**, *16*, 1−4.
(45) Nikitskiy, I.; Goossens, S.; Kufer, D.; Lasanta, T.; Navickaite, G.; Koppens, F. H. L.; Konstantatos, G. Integrating an Electrically Active Colloidal Quantum Dot Photodiode with a Graphene Phototransistor. *Nat. Commun.* **2016**, *7* (May), 1−8.
(46) Gao, J.; Nguyen, S. C.; Bronstein, N. D.; Alivisatos, A. P. Solution-Processed, High-Speed, and High-Quantum-Efficiency Quantum Dot Infrared Photodetectors. *ACS Photonics* **2016**, *3* (7), 1217−1222.

https://dx.doi.org/10.1021/acs.nanolett.0c01614
Nano Lett. XXXX, XXX, XXX−XXX